Tables

Table 1 – Properties of succinonitrile and succinonitrile-camphor alloy.

Succinonitrile	
Molar mass [57]	80.09 g/mol
Latent heat of fusion (ΔH) [57]	3.713 kJ/mol
Liquid density (ρ_L) [17]	970 kg/m^3
Solid density (ρ_S) [17]	1016 kg/m^3
Liquid thermal conductivity (λ_L) [17]	0.223 J/(m.s.K)
Solid thermal conductivity (λ_S) [17]	0.224 J/(m.s.K)
Thermal expansion coefficient (β_T) [58]	7.85x10^{-4} K^{-1}
Kinetic viscosity (v) [59]	2.6 mm^2/s
Succinonitrile-camphor [28]	
Liquidus slope (m_L)	-1.365 K/wt%
Solute diffusion coefficient in the liquid (D_L)	270 µm^2/s
Thermal diffusion coefficient (D_{th})	1.15x10^5 µm^2/s

Table 2 – Interface amplitude at end of solidification (A), under microgravity (µg) and on Earth (1g); experimental interface recoil (Δz_{exp}); experimental corrected interface recoil ($\Delta z_{c,exp}$), using the BBF and KP approaches under microgravity (f_s is the measured solid fraction as defined in the KP model); and simulated recoils using CrysMAS thermal simulations ($\Delta z_{c,num}$). Each measurement has a standard deviation of ±25µm.

	G_1=19 K/cm							G_2=12 K/cm						
	A (µm)							A (µm)						
V_p (µm/s)	µg	1g	Δz_{exp} (mm)	$\Delta z_{c,exp}$ BBF (mm)	f_s	$\Delta z_{c,exp}$ KP (mm)	$\Delta z_{c,num}$ (mm)	µg	1g	Δz_{exp} (mm)	$\Delta z_{c,exp}$ BBF (mm)	f_s	$\Delta z_{c,exp}$ KP (mm)	$\Delta z_{c,num}$ (mm)
0	118	28	---	---	---	---	---	237	56	---	---	---	---	---
0.25	---	---	---	---	---	---	---	625	---	2.65	3.28	---	---	---
0.5	150	125	1.39	1.93	0.92	1.60	---	388	238	2.18	3.35	0.86	2.81	---
1	88	106	1.23	2.04	0.81	1.74	1.32	275	238	1.66	3.10	0.64	2.81	2.12
2	38	63	1.29	2.23	0.62	2.06	1.71	163	188	1.74	3.31	0.66	2.98	2.58
4	-163	50	1.80	2.81	0.69	2.57	2.47	-25	38	2.51	4.15	0.65	3.81	3.48
8	-481	25	3.13	4.17	0.51	4.04	3.89	-350	-63	4.30	5.97	0.86	5.20	5.05

Table 3 – Δz_T values and fitted values of the delay time τ (s) used in the modified WL model considering a BBF and a KP tip undercooling. The Δz_T values are obtained using eq. (13) with the values of $\Delta z_{c,exp}$ listed in Table 2 for each model.

	G_1=19 K/cm				G_2=12 K/cm			
V_p (µm/s)	BBF		KP		BBF		KP	
	Δz_T (mm)	τ(s)	Δz_T (mm)	τ(s)	Δz_T (mm)	τ(s)	Δz_T (mm)	τ(s)
1	0.96	1591	0.66	940	1.39	1998	1.10	1467
2	1.15	637	0.98	492	1.60	837	1.27	564
4	1.73	467	1.49	384	2.44	563	2.10	477
8	3.09	358	2.96	342	4.26	487	3.49	396

Figures

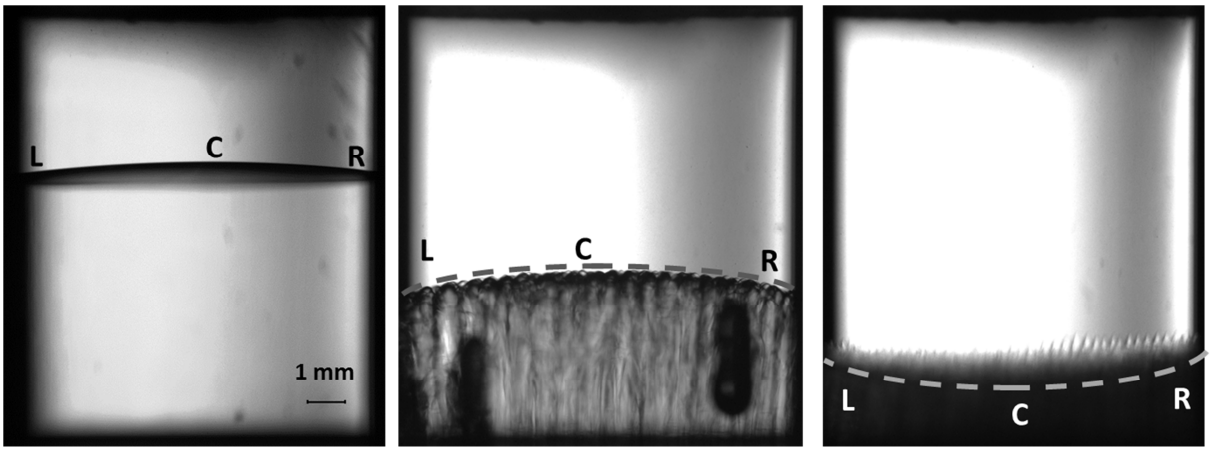

(a) **(b)** **(c)**

Figure 1 – Interface motion measurement method, for G_2=12K/cm: (a) convex without structures at rest; (b) convex with structures at 4µm/s; and (c) concave at 8µm/s.

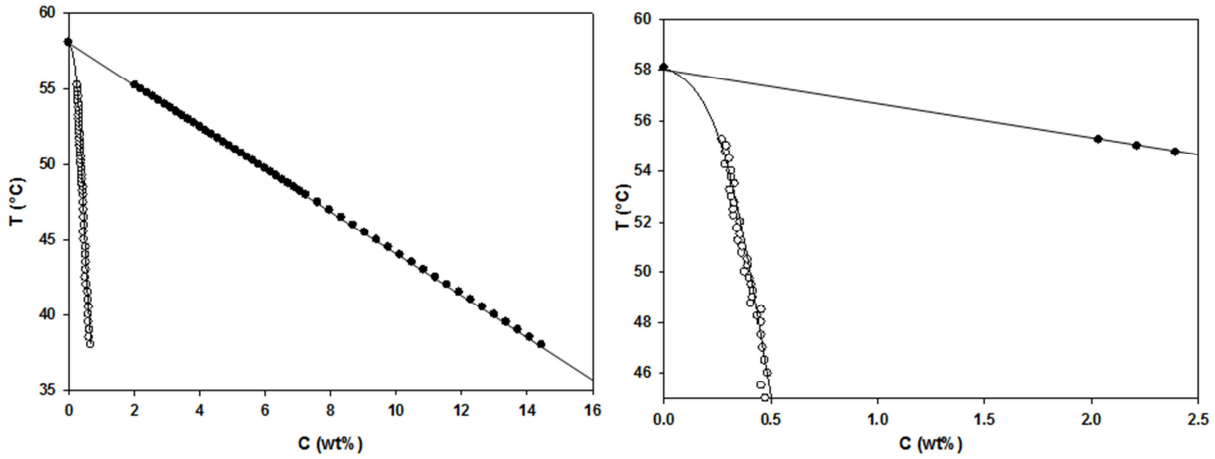

Figure 2 – Phase diagram for the binary system succinonitrile-camphor: ●, *liquidus* and ○, *solidus* lines estimated using fraction of liquid phase measured by Witusiewicz et al.**[31]**.

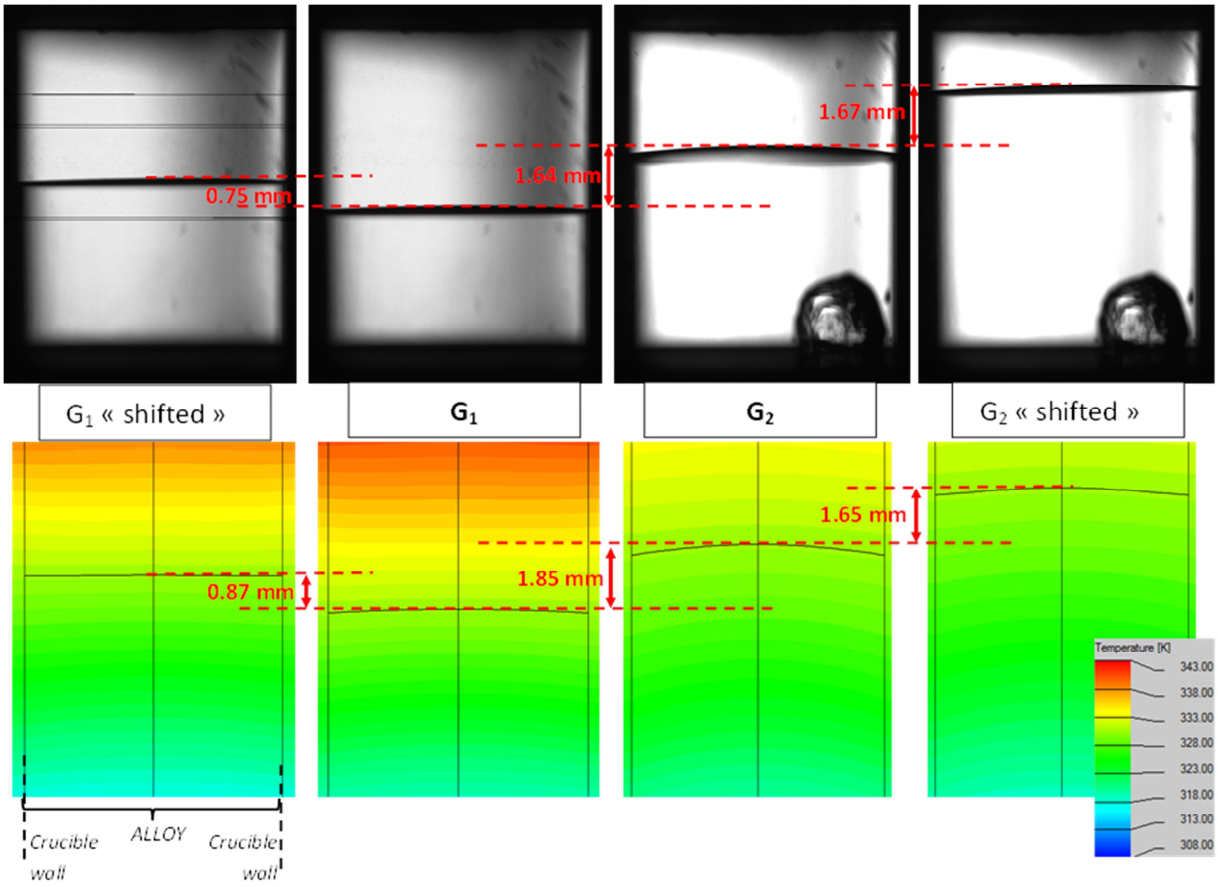

Figure 3 – Interface position and shape for different thermal conditions: experimental images on top are compared to CrysMAS simulations at bottom, with the temperature field as color map. G_1 and G_2 correspond to the nominal control temperatures for the 2 gradients; G_1 shifted and G_2 shifted correspond to the same control temperatures than respectively G_1 and G_2, except that hot zone and booster heater temperatures have been decreased by 2°C.

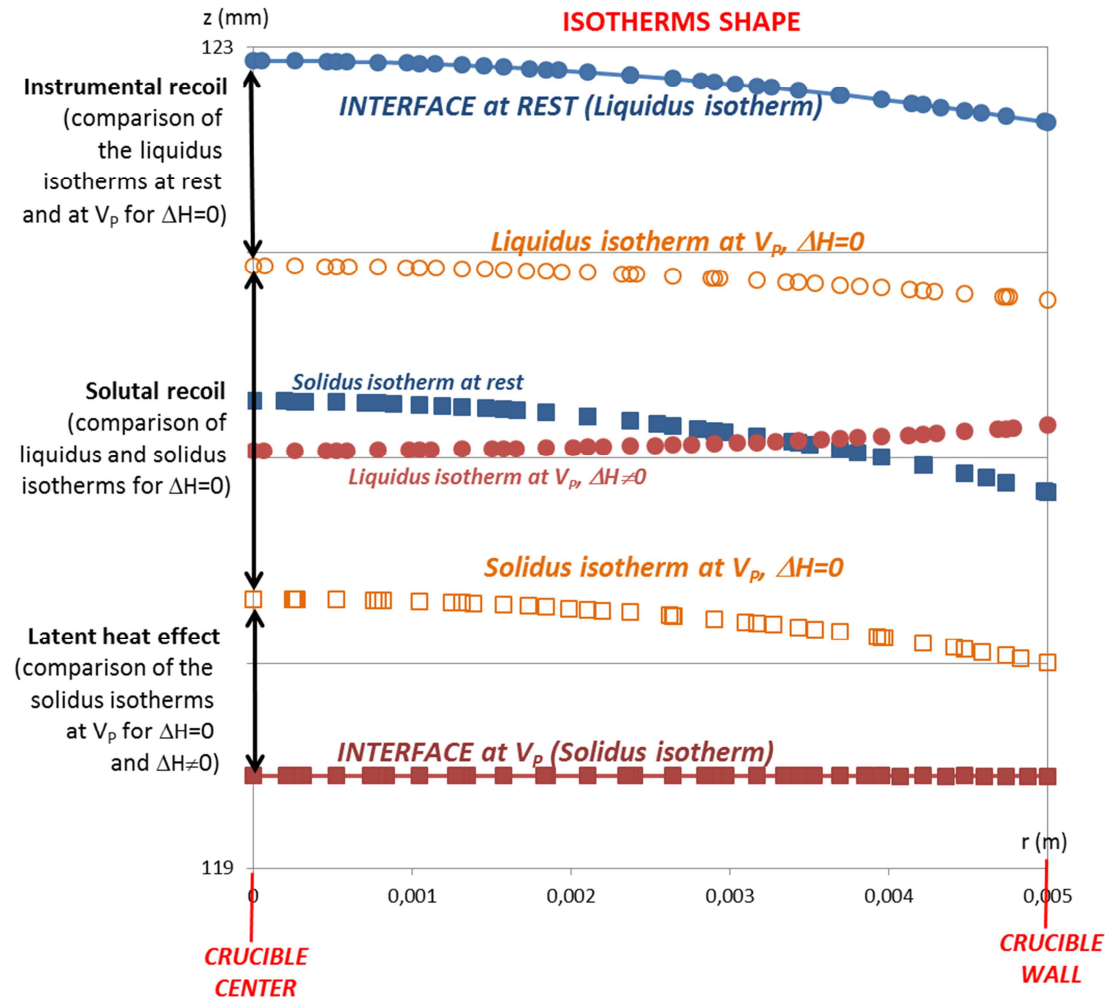

Figure 4 – Position and shape of the *liquidus* and *solidus* isotherms at G_2 = 12 K/cm. In blue: at rest (V_P=0). In orange: at V_P = 4 µm/s with a latent heat $\Delta H = 0$. In red: at V_P = 4 µm/s with $\Delta H \neq 0$.

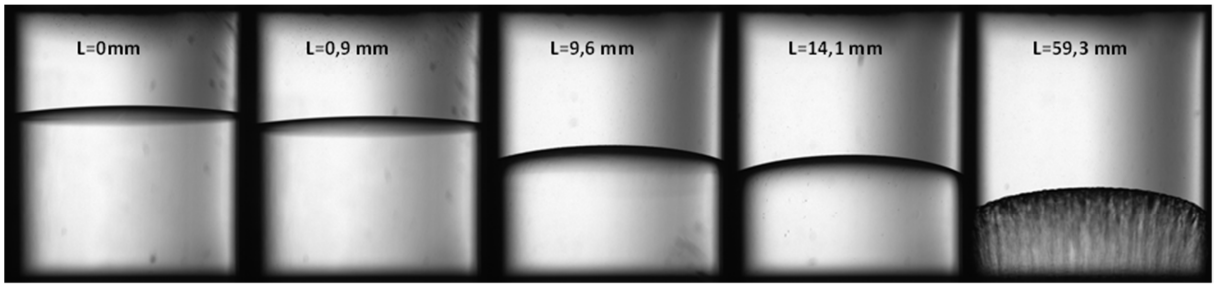

(a)

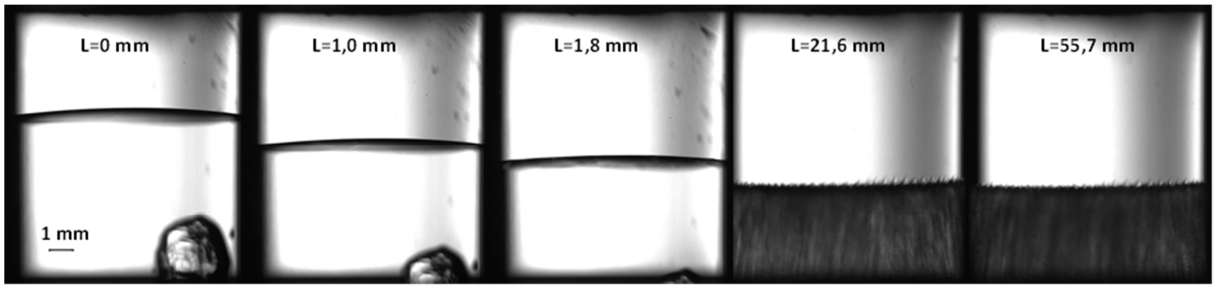

(b)

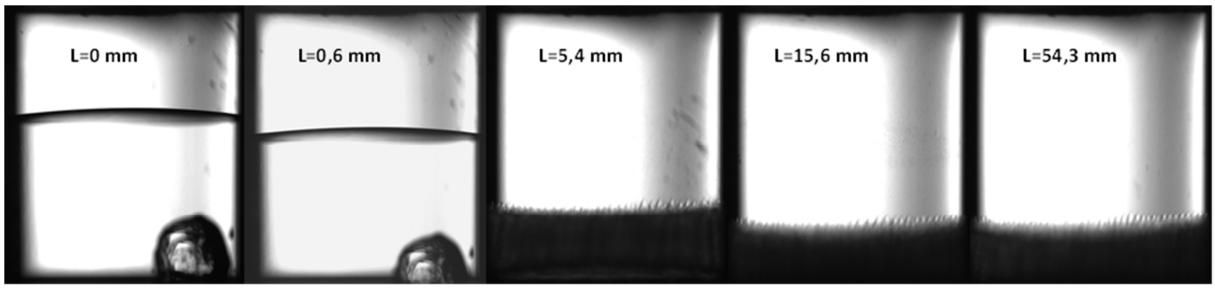

(c)

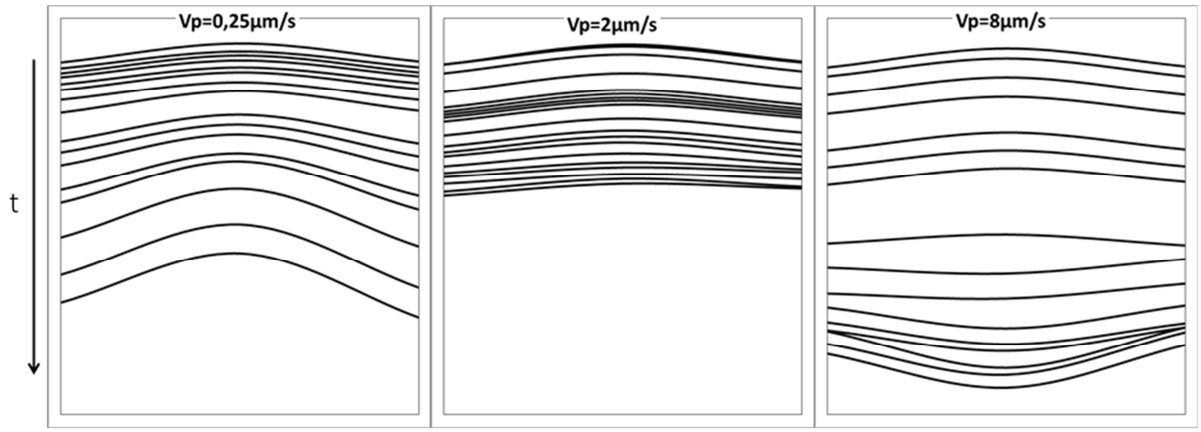

(d)

Figure 5 – Interface evolution from rest to steady state under microgravity at G_2 = 12 K/cm and V_p = (a) 0.25, (b) 4 and (c) 8 µm/s; (d) Schematic representation of interface shape from rest until the end of solidification for three different pulling rates.

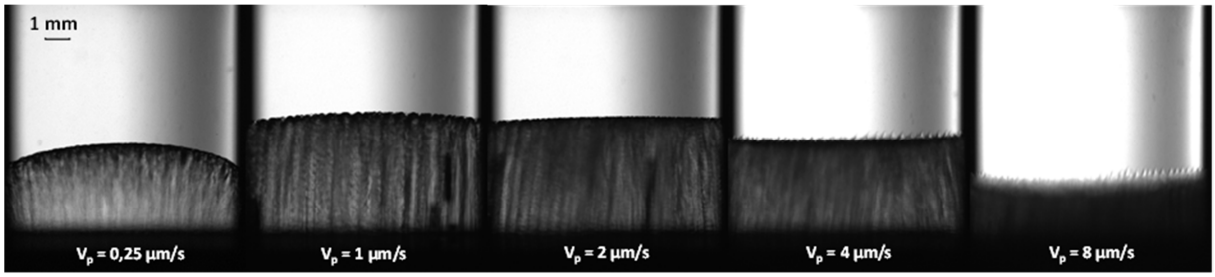

Figure 6 – Steady state interface for different pulling rates at G_2=12K/cm under microgravity.

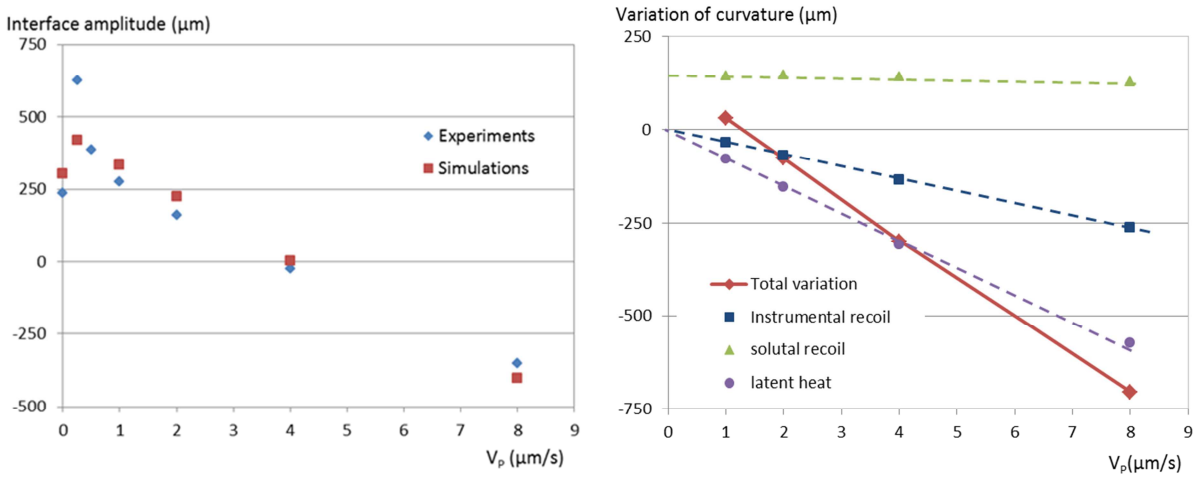

Figure 7 – Analysis of the interface shape with pulling rate (G_2=12 K/cm): a) Comparison of the experimental and numerical interface amplitudes as a function of pulling rate. b) Analysis of numerical data to identify the different contributions to the interface shape change between rest and pulling. Respectively, differences of interface amplitudes are measured between the isotherms shapes: Rest and *Liquidus* at V_P (ΔH=0) for the "Instrumental recoil"; *Liquidus* and *Solidus* at V_P (ΔH=0) for the "Solutal recoil"; *Solidus* at V_P, ΔH = 0 and $\Delta H \neq 0$ for the "Latent heat contribution".

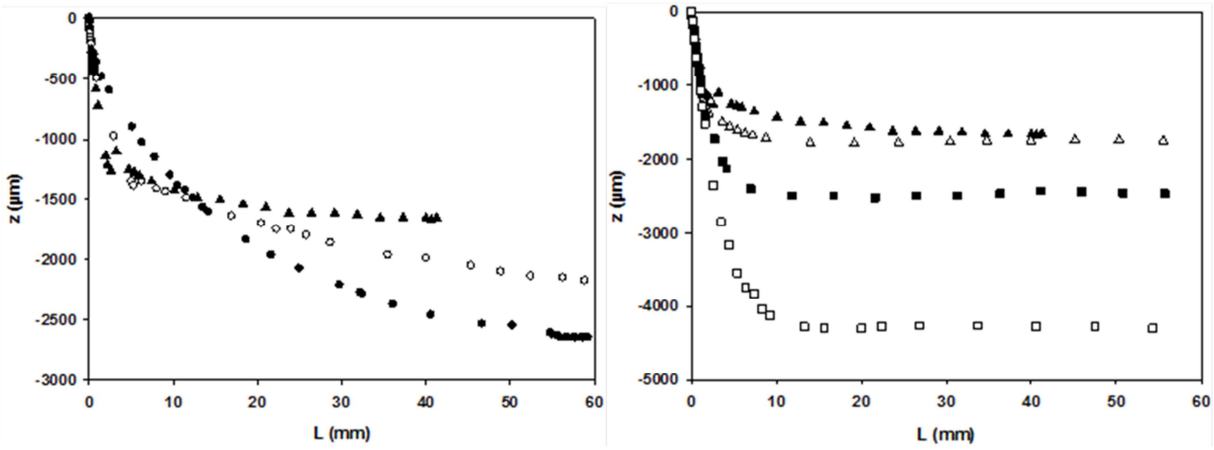

Figure 8 – Interface position (z_0) as a function of solidified length ($L=V_pt$) at G_2=12K/cm for different pulling rates (µm/s): (a) •, 0.25; ○, 0.5; ▲, 1 (b) ▲, 1; Δ, 2; ■, 4; □, 8.

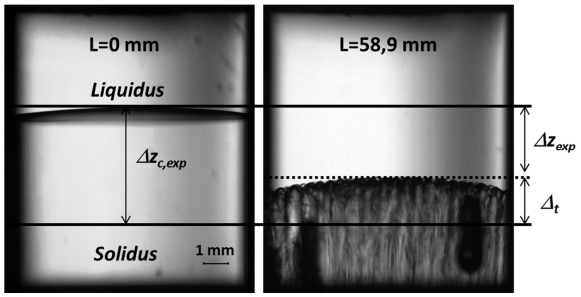

Figure 9 – Schematic representation of interface recoil for V_p=0.5µm/s and G_2=12K/cm, and the corresponding positions of *liquidus* and estimated *solidus*.

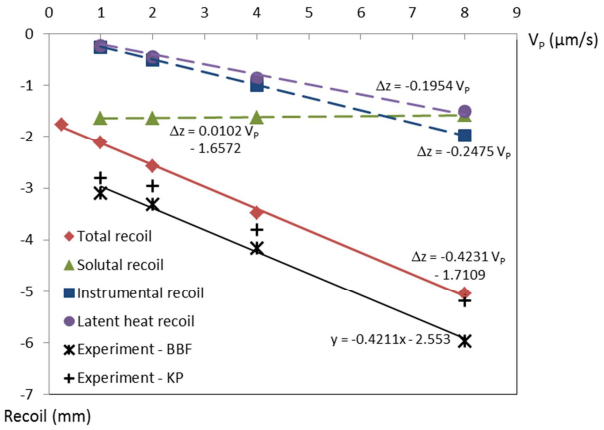

Figure 10 –Analysis of the interface recoil with pulling rate (G_2=12 K/cm): experimental data is given in black, with the BBF and KP calculations for the tip undercooling, and compared to the different recoil contributions identified with numerical simulations.

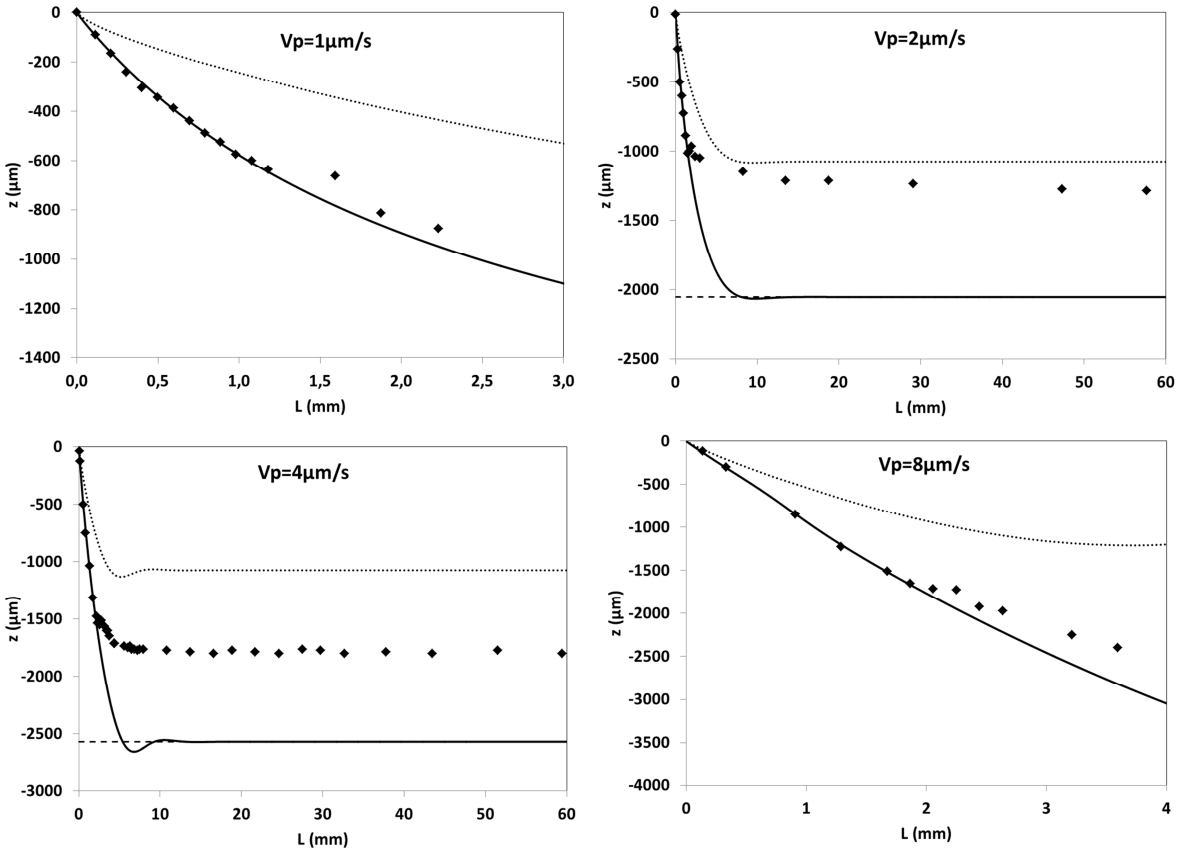

(a)

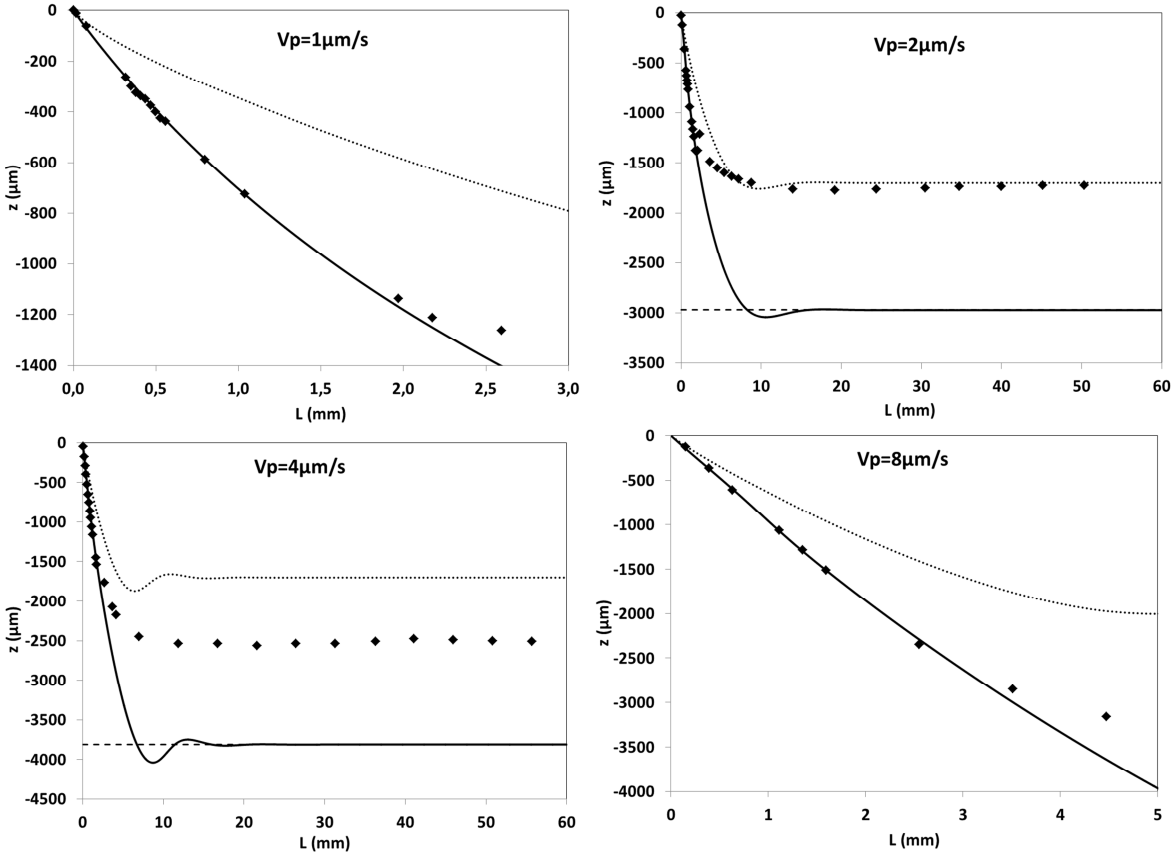

(b)

Figure 11 – Interface position (z_0) as a function of solidified length (L) for different pulling rates: experimental points are superimposed with the modeling results using Warren and Langer [6] model modified to take into account the isotherm shift (full line) and the original model (dotted line), for (a) G_1=19K/cm and (b) G_2=12K/cm. The dashed line corresponds to the estimated *solidus* line.

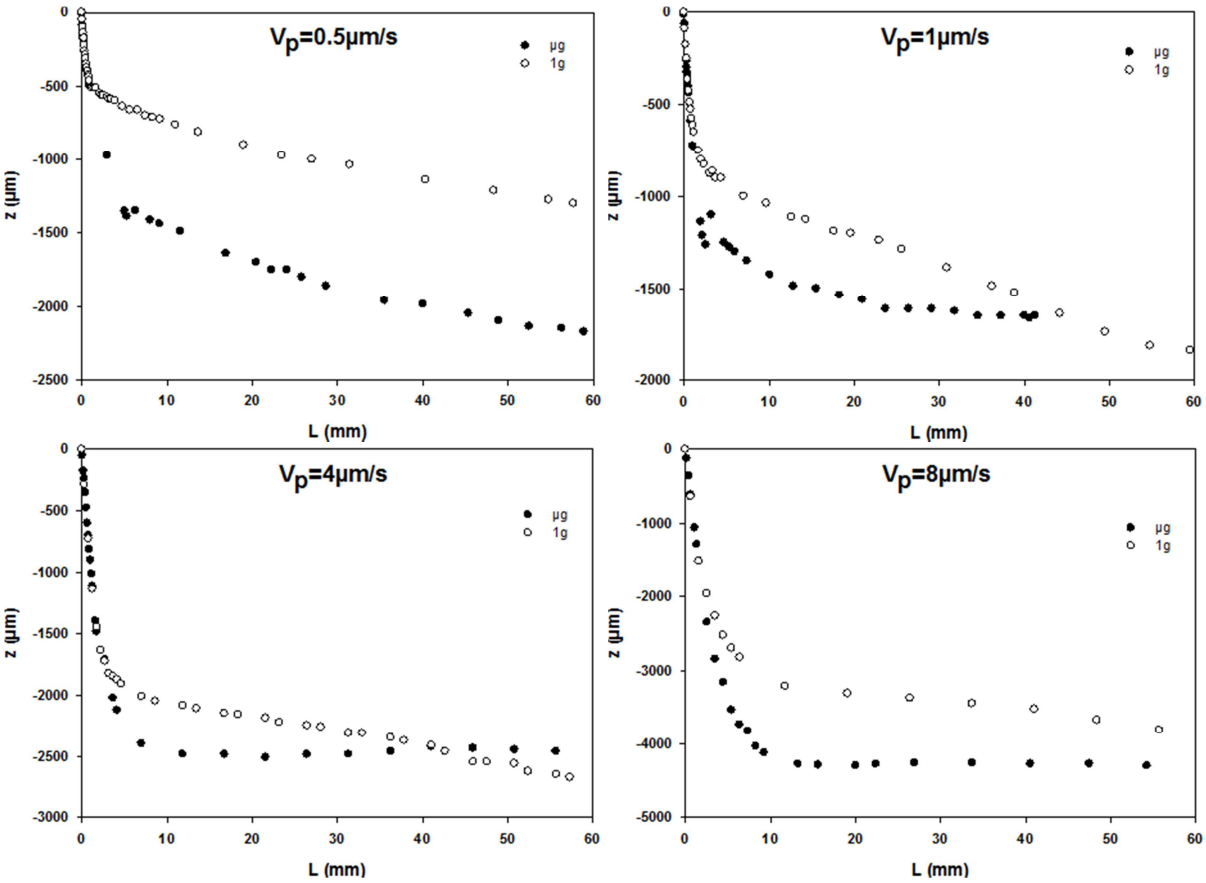

Figure 12 – Interface position (z_0) as a function of solidified length (L) at G_2=12K/cm for different pulling rates onboard ISS (noted "µg") and on ground (noted "1g").

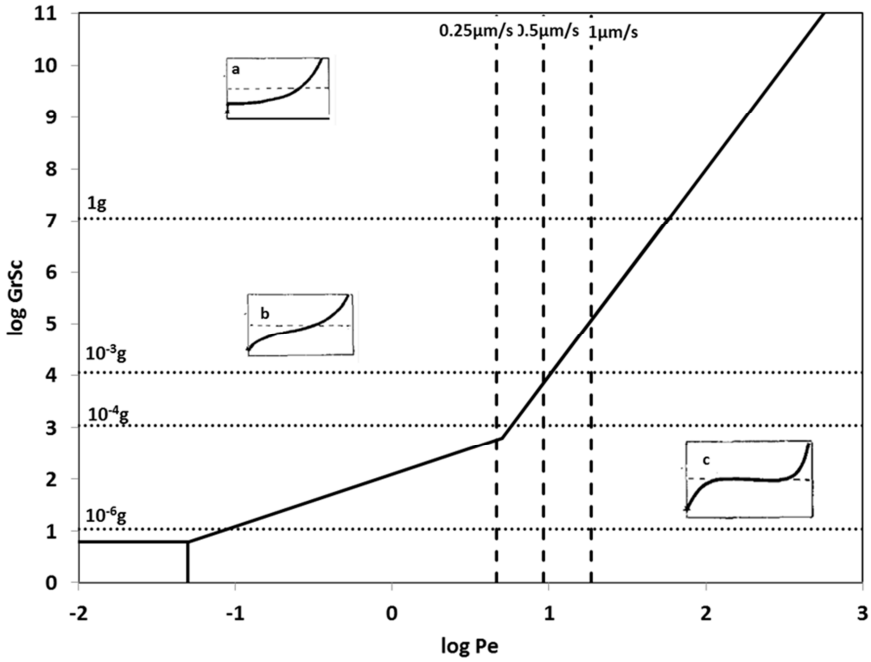

Figure 13 – (Grashof-Schmidt, Peclet) diagram [55, 56] with different segregation profiles shown schematically.